Combining UAV SAR Tomography and Photogrammetry to study an Active Volcanic Vent in Iceland

Alina V. Shevchenko[1], Eduardo Freitas[2], Christian Wimmer[2], Egill Á. Gudnason[3], Magnus T. Gudmundsson[4], Gro B.M. Pedersen[5], Luciano P. de Oliveira[6], Magdalena S. Vassileva[1], Daniel Müller[1], Dibakar K. Ritushree[1,7], Mahdi Motagh[1,7], Thomas R. Walter[1], João Moreira[2], Martin Herold[1], Frieder M. Knabe[8], Gian C. Oré Huacles[9], Hugo E. Hernandez-Figueroa[9]

[1]GFZ Helmholtz Centre for Geosciences, Telegrafenberg, 14473 Potsdam, Germany – (alinash,magda88,dmueller, dibakar,motagh,twalter,herold)@gfz.de
[2]Radaz S.A., São José dos Campos, 12244-000, Brazil – (eduardo.freitas,christian.wimmer,tech)@radaz.com.br
[3]Iceland GeoSurvey ISOR, Urdarhvarfi 8, 203 Kópavogur, Iceland – egill.arni.gudnason@isor.is
[4]Institute of Earth Sciences, University of Iceland, Sturlugata 7, 102 Reykjavík, Iceland – mtg@hi.is
[5]Icelandic Meteorological Office, Bústaðavegur 9, 150 Reykjavík, Iceland – gropedersen@vedur.is
[6]Technology Innovation Institute, Masdar City, SE45 01, Abu Dhabi, United Arab Emirates – luciano.prado@tii.ae
[7]Institute of Photogrammetry and GeoInformation, Leibniz University Hannover, Nienburger Str. 1, 30167 Hannover, Germany
[8]Wissenschaftsladen Potsdam e.V., Friedrich-Engels-Str. 22, 14473 Potsdam, Germany – frieder.knabe@wissenschaftsladen-potsdam.de
[9]School of Electrical and Computer Engineering, University of Campinas, Campinas, 13083-852, Brazil – g228005@dac.unicamp.br, hugo@unicamp.br

Keywords: UAV, SAR Tomography, Photogrammetry, Volcano, Eruption.

Abstract

The recent volcanic unrest on Iceland's Reykjanes Peninsula was an excellent opportunity to better understand volcanic processes and develop hazard mitigation strategies. The eruption was studied using various direct and remote-sensing techniques. Here, we present an innovative UAV-based TomoSAR approach application, combined with photogrammetry, to explore the external and internal structures of an active volcanic vent within the Sundhnúkur crater row, where nine eruptions have occurred since December 2023. The surveys were conducted on 20 May 2024 (12 days after the end of the March–May eruption) and on 1 August 2024 (40 days after the May–June eruption). For optical data collection, we used a DJI Mavic 3T quadcopter, equipped with an RGB camera and an infrared sensor. The radar data were acquired using a UAV-based interferometric SAR system, Explorer RD350, which is capable of collecting P-band data in helical-trajectory mode. The optical data were processed using the standard photogrammetric workflow, and the SAR data were processed using the Refractive Back Projection algorithm, which enabled the extraction of amplitude images as slices at given depths with a ground penetration of up to 20 m. Our results show that the higher-intensity areas in the subsurface images correspond to the vent's crater center, while the lower-intensity areas correspond to the slopes of its cinder cone, composed of loose volcanic material. We assume that the higher-intensity areas in the amplitude images represent structures of denser material at depth, e.g., a lava conduit within the volcanic cone.

1. Introduction

Aerial photogrammetry has been used to study volcanoes for several decades, dating back to the mid-20th century (Dvigalo et al., 2016). It was successfully applied to monitor ongoing (at that time) eruptions, e.g., on La Palma, Spain (Walter et al., 2023) and Reykjanes, Iceland (Pedersen et al., 2022), as well as to reveal hazardous events that occurred at volcanoes several decades ago, e.g., in Askja caldera, Iceland (Shevchenko et al., 2024). Volcanoes are particularly interesting objects to investigate with comparative photogrammetric analysis, as they are highly dynamic landforms that can drastically change their edifices over short timescales (Shevchenko et al., 2020). Unmanned Aerial Vehicles (UAVs) are increasingly used in volcanological research, enabling independent, safe data collection in the hazardous environments of active volcanoes (James et al., 2020).

Synthetic Aperture Radar Tomography (TomoSAR) (Fornaro et al., 2024) is a recent technique with the potential to significantly advance volcanological research, particularly when using P-band sensors (wavelength 0.3–1.0 m), which enable subsurface exploration. So far, UAV-based P-band TomoSAR has been successfully used to detect ant nests (Oré et al., 2022), locate buried bodies (Oré et al., 2024), analyze tree roots in boreal forest (Persson et al., 2024), etc. Here, for the first time, we present the application of the UAV P-band TomoSAR approach, combined with photogrammetry, to study the external and internal structures of an active volcanic vent within the Sundhnúkur crater row on the Reykjanes Peninsula in Iceland (Figure 1).

Iceland is one of the most active volcanic regions in the world, with frequent fissure eruptions. The recent unrest on the Reykjanes Peninsula began in January 2020 with intense seismicity and inflation (Flóvenz et al., 2022); the first eruption occurred within the Fagradalsfjall volcanic complex in March 2021, followed by two more eruptions in 2022 and 2023 in the area (Troll et al., 2024). In December 2023, eruptive activity emerged approximately 6 km west of Fagradalsfjall, at the Sundhnúkur crater row in the Svartsengi volcanic system (Parks et al., 2025). Since then, nine eruptions have occurred at Svartsengi, and further eruptions can be expected.

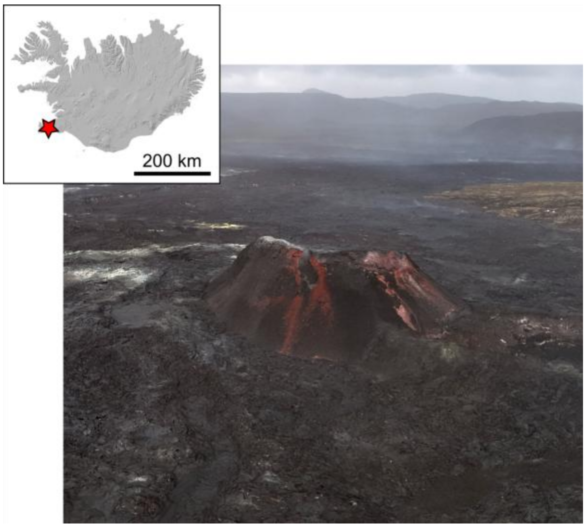

Figure 1. The explored volcanic vent within the Sundhnúkur crater row; UAV photo from 1 August 2024, view from the west. The inset shows the location of the vent in Iceland.

2. Methods

2.1 Data acquisition

To study the Sundhnúkur active vent, we used optical and SAR UAV sensors. The surveys were conducted on 20 May 2024 (12 days after the end of the March–May eruption) and on 1 August 2024 (40 days after the May–June eruption). The launching point was established on a lava flow protection barrier (Pinter et al., 2026) ~1 km away from the vent.

For optical data collection, we used a DJI Mavic 3T Real-Time Kinematic (RTK) quadcopter, equipped with a 48 MP ½″ CMOS camera and infrared sensor (8–14 µm thermal infrared range). We performed automatic mapping of the area at a fixed flying height of 120 m from the launching point.

The radar data were acquired with the UAV-based interferometric SAR system, Explorer RD350 (Figure 2), which operates in three bands (C, L, and P) and three modes (linear, circular, and helical) (Pantoja et al., 2022). For our ground-penetrating TomoSAR purposes, we used only P-band acquisitions (frequency – 400 MHz) conducted in helical-trajectory mode (Figure 3). The automated helical flights were performed at heights ranging from 120 m to 80 m, with two and a half loops and a gradually increasing radius from 150 m to 230 m, focusing on the vent and capturing an area of 1.42 Ha. Data referencing was performed in real-time mode with the pre-flight installation of the GNSS ground station (GS).

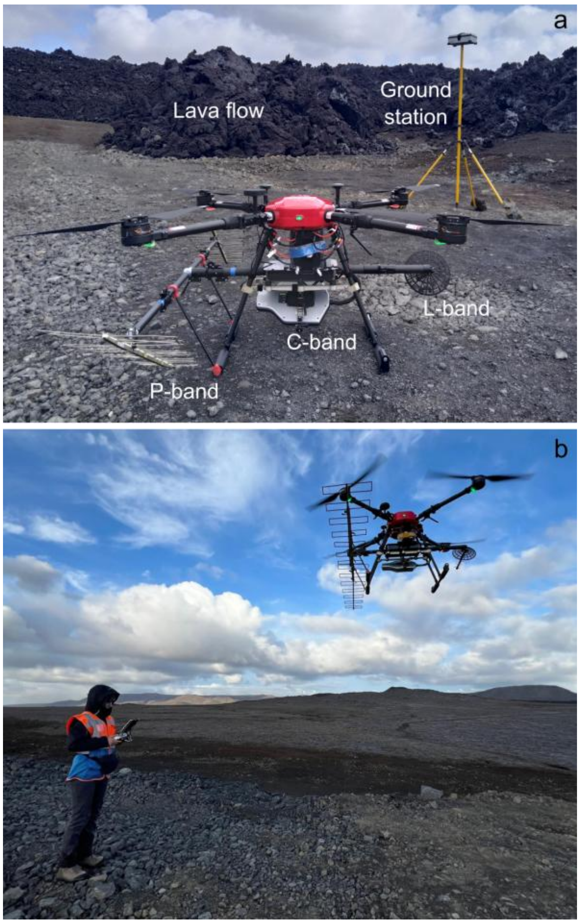

Figure 2. Employment of Explorer RD350 in Iceland to study volcanic unrest: a. Explorer RD350 with the ground station at the recently emplaced lava flow; b. The author is launching the drone to survey the vent.

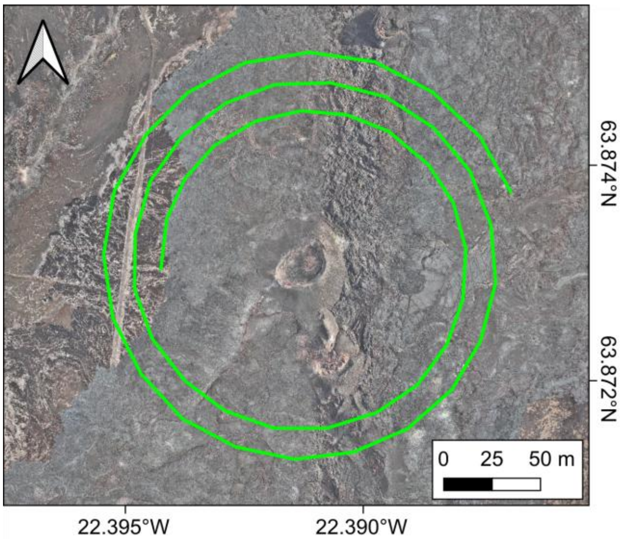

Figure 3. Map view of the helical flight trajectory of Explorer RD350 over the Sundhnúkur vent; the map base is orthomosaic generated from the 20 May 2024 optical survey data.

https://doi.org/10.5194/isprs-archives-XLIX-B3-2026-257-2026 | © Author(s) 2026. CC BY 4.0 License.

2.2 Data processing and analysis

The general processing workflow is presented in the flowchart (Figure 4). The optical data were processed using the standard photogrammetric workflow in Agisoft Metashape v. 2.0.2 (Civico et al., 2024), which includes the following steps: (i) manual data quality check with exclusion of all blurry images and uploading high-quality georeferenced photos to Metashape; (ii) camera alignment with overlapping image matching and triangulation to obtain camera positions and orientations; (iii) generation of depth maps and sparse point clouds with automated Multi-View Stereo (MVS) technique; (iv) extraction of final products – dense point clouds, Digital Elevation Models (DEMs), and visible and infrared orthomosaics of 2–5 cm resolution. Before DEMs generation, the point clouds were cleaned in Metashape by removing isolated points, which improved the DEMs’ quality.

The P-band SAR data were processed using a workflow developed by the Explorer RD350 manufacturer, which comprises several main steps described below.

(i) Preparation of raw data and processing parameters, i.e., conversion of the ground station and drone GNSS files into specific file formats using the RTKCONV program within the open-source RTKLIB package; obtaining precise coordinates of the ground station in the RTKPOST program using a permanent GNSS station as a base, in this case – Reykjavik station (REYK00ISL); and obtaining refractive index of the surveying material, in this case – of basaltic lava. The refractive index was obtained as the square root of the effective dielectric constant, which was laboratory-measured from the Sundhnúkur eruption lava samples collected in the field.

(ii) Pre-processing, which includes environment setup, i.e., data allocation into specific directories; automated data quality check and corrections, e.g., cutting of the radar data to remove parts from the time when the drone was still on the ground, which can influence the processed image quality; and range compression to increase spatial resolution. The last two procedures were automatically performed in the GNU Data Language (GDL) program ‘proz,/heli’ developed by the Explorer RD350 manufacturer.

(iii) Batch configuration allows customizing processing by entering required parameters and automates the workflow by sequentially executing numerous commands. The following parameters were set for the automated processing: coverage area – 200×200 m, horizontal resolution – 20 cm, vertical resolution – 1 m, and refractive index of basaltic lava – 1.9. In this step, we also created a link to the photogrammetrically derived UAV DEM, which was used in the next step to improve the accuracy of the amplitude images, following Rocha et al. (2025).

(iv) Refractive Back Projection (RBP) is a time-domain algorithm that enables the extraction of amplitude images as slices at given depths, with a ground penetration of up to tens of meters, depending on the medium's scattering properties. Unlike frequency-domain algorithms, it handles arbitrary flight paths and produces geocoded images; however, it requires an accurate DEM and substantial computational resources. Moreover, RBP accounts for the refraction effect in subsurface imaging and allows processing with a refractive index other than 1, which is essential in our case. We used the RBP algorithm's automatic implementation in the GDL program ‘back’ developed by the Explorer RD350 manufacturer. The main steps of the algorithm – definition of the image sample grid, calculation of the slant range and fractional range index, and data interpolation and accumulation into the sample grid – are described in detail in previous studies (Xu et al., 2023; Góes et al., 2023).

In the RBP algorithm, a DEM is primarily used to model the acquisition topography, ensuring precise focusing of SAR data, especially in complex or rugged terrain. A DEM enables the algorithm to compute precise distances from the sensor to each pixel in the scene, thereby preventing distortion caused by topographic variations (Rocha et al., 2025). In cases of stable topography in the survey area, for example, the NASA Shuttle Radar Topography Mission (SRTM) can be utilized in RBP for topographic correction. However, in our case, it wasn't applicable because the topography changed significantly due to the eruption, and DEMs from the same surveying days were necessary. Therefore, we applied topographic correction using the DEMs obtained with optical UAV (see above).

(v) As a final product of TomoSAR processing, we obtained a stack of 21 amplitude images per acquisition: one surface image and 20 subsurface images with 1-m vertical resolution and 20-m ground-penetrating depth.

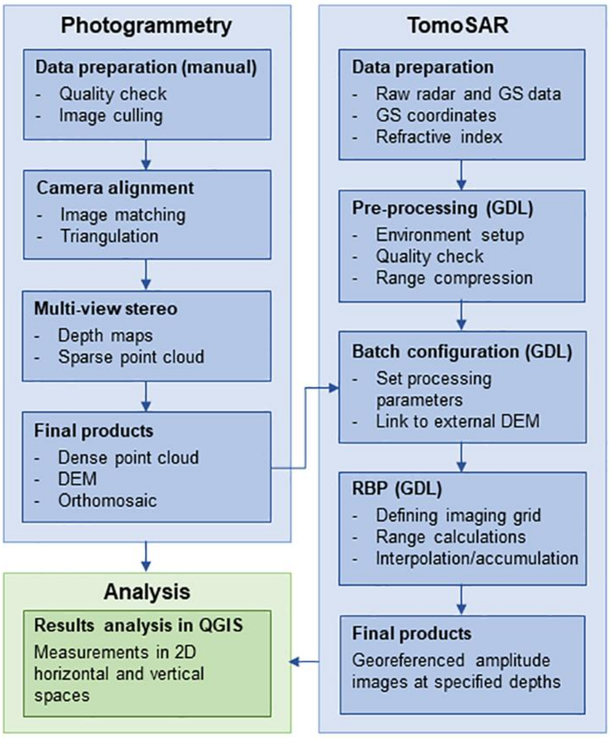

Figure 4. The general workflow chart shows the main steps of photogrammetric and TomoSAR processing, and their combination to study the surface and subsurface features of the Sundhnúkur vent.

The optical DEMs and orthomosaics, together with P-band TomoSAR amplitude images, were analyzed and compared in QGIS v. 3.44.7. The infrared data were analyzed using DJI Thermal Analysis Tool v. 3.1.0. The higher-intensity areas in the amplitude images generated at specific depths were measured in 2D horizontal and vertical spaces relative to topographic features identified in the optical DEMs and orthomosaics.

3. Results

Our surveys focused on the largest vent within the new Sundhnúkur crater row, which was active during the fourth eruption from 16 March to 8 May 2024 and the fifth eruption from 29 May to 22 June 2024; morphologically, this vent is a cratered cinder cone (Figure 5–8). The resulting DEM from optical data acquired on 20 May 2024 (Figure 5a) shows that the cone reached a maximum height of 20 m relative to the surrounding lava field, with a foot diameter of ~100 m. The elongated crater had a rim measuring 42 × 58 m and a depth of 14 m. The DEM from our survey conducted on 1 August 2024 (Figure 5b) shows that the cone's relative height reached a maximum of 27 m, and the surrounding lava field level rose by an average of 10 m. The foot diameter increased to ~112 m, and the new elongated crater rim dimensions were 53 × 75 m. The crater reached 25 m in depth, measured from the highest point of the rim (in the NW part). The center of the crater has shifted ~15 m towards SW since 20 May 2024, which is not visible in Figures 5–8 between (a) and (b) because all maps were centered according to the center of the crater.

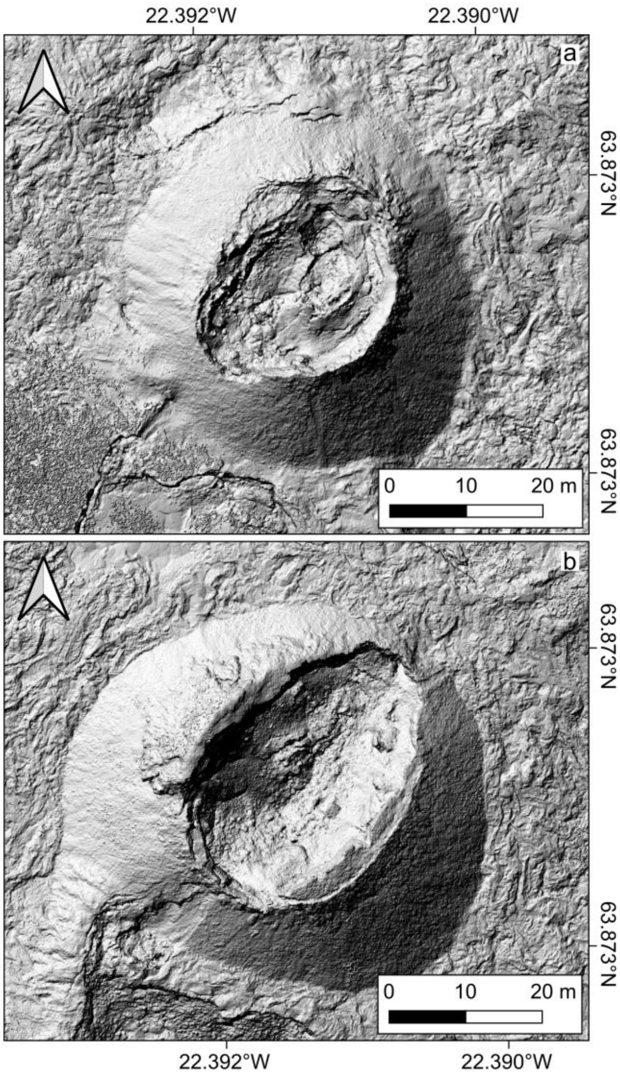

Figure 5. Hillshade visualizations of the DEMs from the optical UAV surveys of the Sundhnúkur cinder cone on 20 May (a) and 1 August (b) 2024, showing two stages of the cone morphological development, with one eruption in between.

The processing of infrared data revealed that on 20 May 2024, the maximum apparent surface temperature within the crater was ~400°C, 12 days after the eruption (Figure 6a). The thermal anomalies are mainly observed along the crater rim and on the crater's inner walls, possibly due to the constant crumbling of cooled surface material in steep, unstable parts of the crater, exposing hot rock. Moreover, the hot gas might preferentially rise through the rim rather than the crater center, causing higher temperatures along the rim, since rims are much more porous and therefore provide a preferred pathway for hot steam/gas. The crater floor appeared to be mostly at relatively low temperatures (from ~5°C to ~30°C), most likely due to the crust formed atop the conduit lava. On 1 August 2024, the highest apparent surface temperature, mostly observed along the crater rim, was ~290 °C, 40 days after the next eruption (Figure 6b). The thermal anomalies are attributed to parts of the crater rim where sagging is also observed in the DEM (Figure 5b). The crater floor appeared to be, again, at relatively low temperatures (from ~10°C to ~40°C).

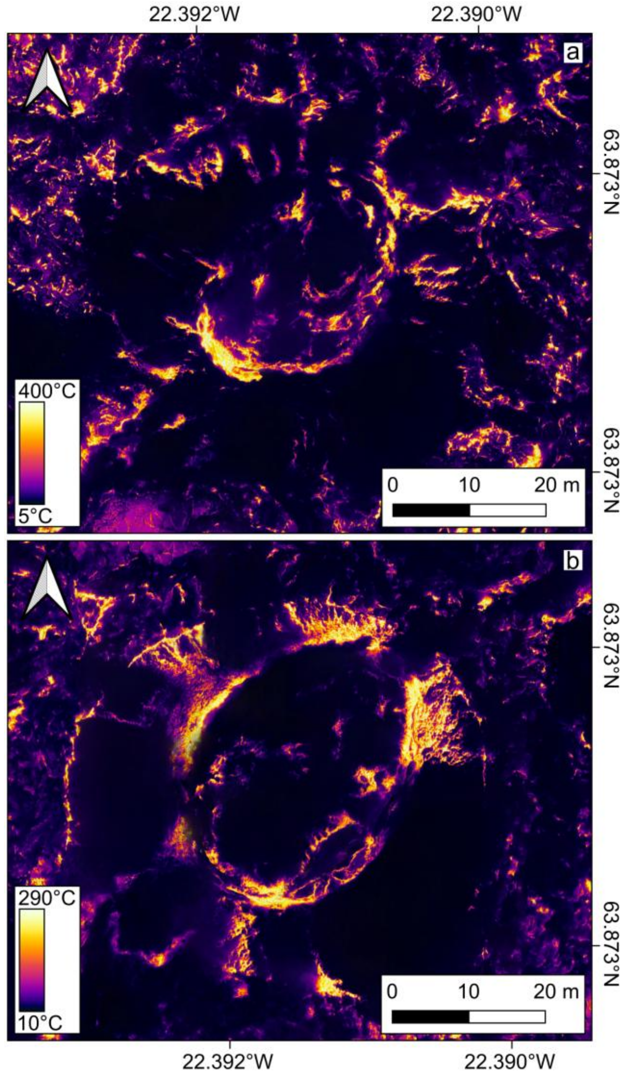

Figure 6. Infrared orthomosaics generated from UAV data acquired on 20 May (a) and 1 August (b) 2024, showing thermal anomalies inside the crater and on the outer slopes of the Sundhnúkur cone.

The TomoSAR results show higher- and lower-intensity areas in the amplitude images. In the 20 May 2024 surface image (Figure 7a), the higher-intensity (brighter) areas correspond to the slopes with a small Local Incidence Angle (angle between the radar beam and the surface normal, LIA), such as the SE crater wall, while the lower-intensity (darker) areas correspond to more horizontal surfaces, such as several flat areas on the surrounding lava field or crater floor. The further 1–20 m subsurface amplitude images show a gradual transition in the higher-intensity area at the center of the cone from repeating elongated crater floor outlines to a more circular structure, as shown in the image at 13-m depth (Figure 8a). This higher-intensity central area is surrounded by a lower-intensity area, which corresponds to the slopes of the cinder cone. The images, generated at depths of 13–20 m, reveal a gradual ~11 m migration of the higher-intensity area to the NW. The surface amplitude image from 1 August 2024 (Figure 7b) shows that slopes with small LIA appear as higher-intensity areas, like those in the previous set. The subsurface images, however, reveal a gradual transition of the higher-intensity central area into a NE–SW linear structure, which aligns with the elongated crater bottom, as shown in the image at a depth of 13 m (Figure 8b). The images representing depths of 8–20 m show a gradual ~17 m shift of the linear structure towards the SE.

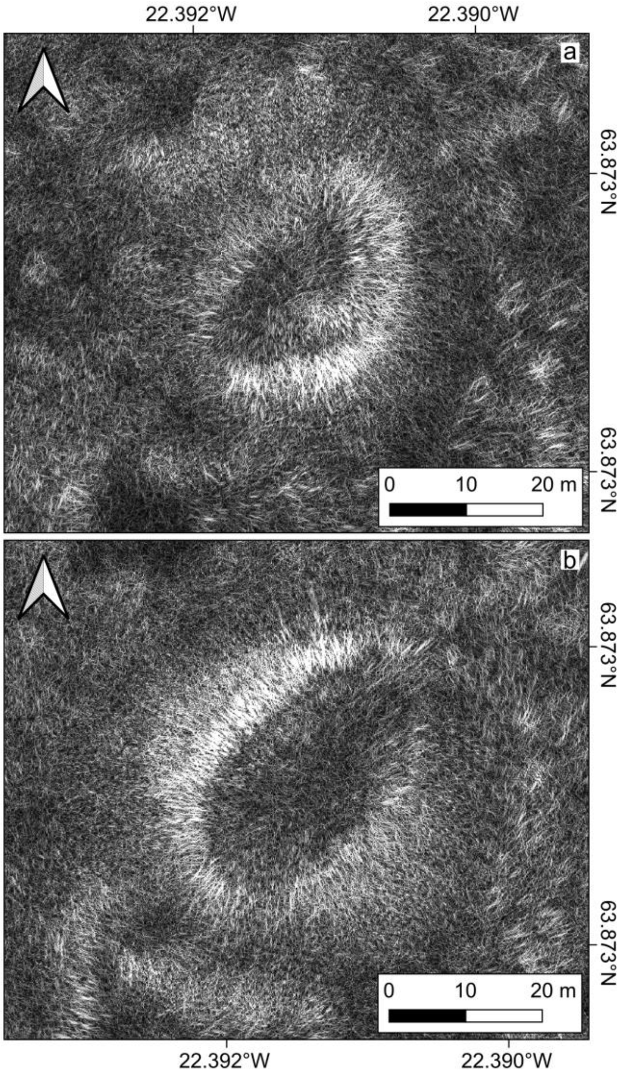

Figure 7. Results of the SAR UAV surveys of the Sundhnúkur cinder cone on 20 May (a) and 1 August (b) 2024; amplitude surface images generated using the P-band TomoSAR approach showing surfaces with a small LIA as higher-intensity areas.

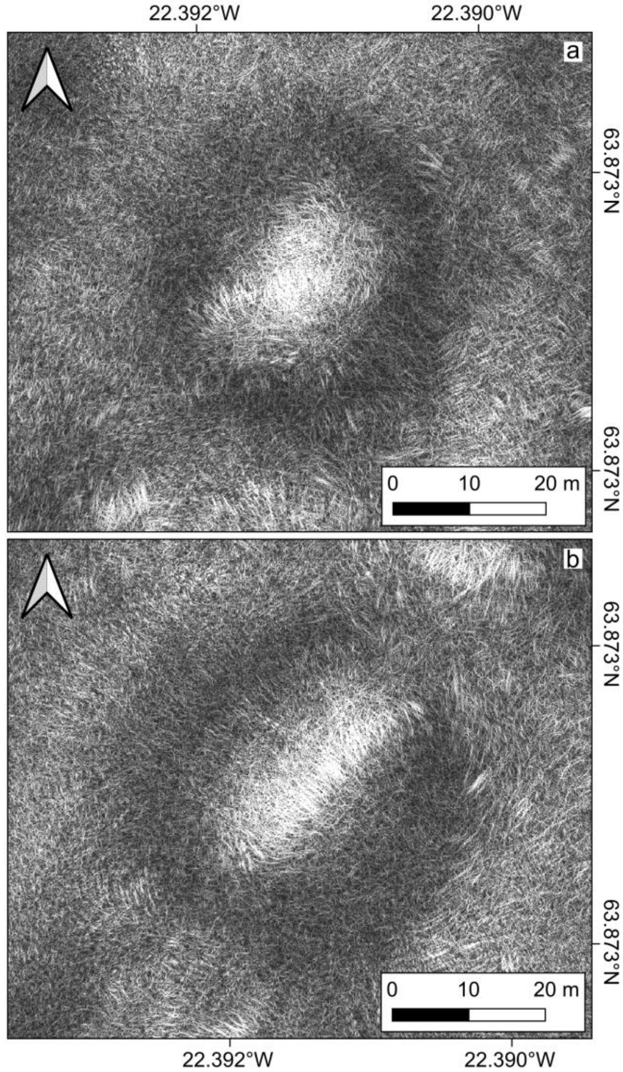

Figure 8. Results of the SAR UAV surveys of the Sundhnúkur cinder cone on 20 May (a) and 1 August (b) 2024; amplitude images at a depth of 13 m likely reveal the conduit structure as a higher-intensity area in the center.

4. Discussion

Since the higher intensity areas in the subsurface amplitude images are attributed to the center of the crater, and lower intensity areas correspond to the slopes of the cinder cone (Figure 8), we can infer that the higher intensity areas can represent denser lava in the conduit, while the lower intensity areas can show lower density material of the cinder cone, i.e., scoria that had been ejected during the eruptions. The higher-density materials have higher refractive indices (Oré et al., 2024), which explains why the transition from loose to dense volcanic material can be visible in the TomoSAR amplitude images. However, the high post-eruption temperatures of lava could reduce its density and, consequently, its refractive index; nevertheless, the density of even liquid lava (which solidifies at 800° C – 1,000° C) is higher than that of scoria. Additionally, the bedding angle of the surface/subsurface material can influence reflectance, and since volcanic conduits or dikes typically have a near-vertical orientation, we suggest that our findings reflect two stages in the development of the Sundhnúkur crater conduit.

https://doi.org/10.5194/isprs-archives-XLIX-B3-2026-257-2026

The DEM comparison revealed a ~15 m shift of the crater center (and the whole cone) to the SW after the May–June 2024 eruption. This shift is in alignment with the general orientation of the Sundhnúkur crater row and the May–June 2024 eruption fissure (NE–SW), which crosscut the cone; however, it is perpendicular to the NW–SE gradual shifts of the higher-intensity areas revealed in the subsurface amplitude images. This observation requires further analysis using 3D subsurface visualizations, which will be the next stage of our research.

To the best of our knowledge, this work is the first to apply the P-band UAV TomoSAR approach to active volcanic structures, which is also a major limitation, because there are no comparable examples. Moreover, ground truthing, an essential part of remote sensing research, was not possible in our case due to the hazardous environment of the investigated object. One way to validate our results would be to compare them with the results of other aerial approaches with ground-penetrating capabilities applied during or shortly after an eruption, e.g., aeromagnetic or Very Low Frequency (VLF) electromagnetic methods.

5. Conclusions

(i) For the first time, we applied a ground-penetrating P-band UAV TomoSAR approach to an active volcanic vent.

(ii) We assume that the higher-intensity areas in the amplitude images can represent structures of denser material at depth, e.g., a lava conduit inside a cinder cone.

(iii) Our results may indicate that the orientation angle of the transient zones between materials with different reflectance properties could also affect the representation of subsurface objects.

(iv) We suggest that it is crucial to combine ground-penetrating P-band data collection with optical surveys to compare the surface and subsurface structures. Moreover, it is especially necessary for dynamic objects such as active volcanoes, since their topography can change substantially during an eruption, and global DEMs (such as SRTM), which are usually used for topographic correction in the RBP algorithm, do not represent the actual surface.

(v) The innovative application of the UAV-based P-band TomoSAR in volcanological research presented here has a limitation: it is impossible to obtain ground-truth data during or shortly after an eruption. Comparisons with other UAV-based geophysical surveys can serve as a means of validation.

Acknowledgements

We acknowledge the Icelandic Centre for Research (Rannís) for issuing the research permit, GFZ Helmholtz Centre for Geosciences and Radaz S.A. for financing the fieldwork, Christin Skala (GFZ) for assistance with equipment transportation, and Sen Lyu (GFZ) for discussions on methodology. This study is a contribution to the Discovery Fellowship Project VolcIce funded by GFZ. The contributions of Gian Oré Huacles and Hugo Hernandez-Figueroa were supported by FAPESP (Grant No. 2022/13498-6) and CNPq (Grant No. 314539/2023-9).

References

Civico, R., Ricci, T., Cecili, A., Scarlato, P., 2024: High-resolution topography reveals morphological changes of Stromboli volcano following the July 2024 eruption. *Sci. Data*, 11, 1219. doi.org/10.1038/s41597-024-04098-y.

Dvigalo, V., Shevchenko, A., Svirid, I., 2016: Photogrammetric survey in volcanology: a case study for Kamchatka active volcanoes. In: *Updates in volcanology – from volcano modelling to volcano geology*. Intech Open. doi.org/10.5772/63577.

Flóvenz, Ó.G., Wang, R., Hersir, G.P., Dahm, T., Hainzl, S., Vassileva, M.S., Drouin, V., Heimann, S., Isken, M.P., Gudnason, E.Á., Ágústsson, K., Ágústsdóttir, T., Horálek, J., Motagh, M., Walter, T.R., Rivalta, E., Jousset, P., Krawczyk, C.M., Milkereit, C., 2022: Cyclical geothermal unrest as a precursor to Iceland’s 2021 Fagradalsfjall eruption. *Nat. Geosci.*, 15, 397–404. doi.org/10.1038/s41561-022-00930-5.

Fornaro, G., Schirinzi, G., Pauciullo, A., Pascazio, V., Reale, D., 2024: SAR tomography. In: *Multi-Dimensional Imaging with Synthetic Aperture Radar*. Elsevier. doi.org/10.1016/B978-0-12-821655-2.00012-7.

Góes, J.A., Oré, G., Lukin, K.A., Hernandez-Figueroa, H.E., 2023: Refraction Effect in SAR Processing for Focused Subsurface Tomography. *2023 SBMO/IEEE MTT-S International Microwave and Optoelectronics Conference (IMOC)*, 256–258. doi.org/10.1109/IMOC57131.2023.10379707.

James, M.R., Carr, B., d’Arcy, F., Diefenbach, A.K., Dietterich, H.R., Fornaciai, A., Lev, E., Liu, E.J., Pieri, D.C., Rodgers, M., Smets, B., Terada, A., von Aulock, F.W., Walter, T.R., Woodo, K.T., Zorn, E.U., 2020: Volcanological applications of unoccupied aircraft systems (UAS): Developments, strategies, and future challenges. *Volcanica*, 3/1, 67–114. doi.org/10.30909/vol.03.01.67114.

Oré, G., Freitas, E., Wimmer, C., Hernandez-Figueroa, H.E., de Vicente, K.K., Machado, J., 2024: Locating Buried Bodies Using SAR Tomography. *IGARSS 2024 – 2024 IEEE International Geoscience and Remote Sensing Symposium*, 1964–1966. doi.org/10.1109/IGARSS53475.2024.10641906.

Oré, G., Santos, A., Ukan, D., Zanetti, R., Camargo, M., Oliveira, L.P., Hernandez-Figueroa, H.E., 2022: Ant Nests Detection in Industrial Forests by SAR P-Band Tomography. *IGARSS 2022 – 2022 IEEE International Geoscience and Remote Sensing Symposium*, 4791–4794. doi.org/10.1109/IGARSS46834.2022.9884086.

Pantoja, J.J., Vega, F., Prado, L., Yang, O., AlAli, B., Kasmi, C., Moreira, L., Lübeck, D., Wimmer, C. 2022: Drone-Borne Synthetic Aperture Radar for GPR Applications: Buried Pipe Inspection. *2022 3rd URSI Atlantic and Asia Pacific Radio Science Meeting (AT-AP-RASC)*, 1–2. doi.org/10.23919/AT-AP-RASC54737.2022.9814274.

Parks, M., Drouin, V., Sigmundsson, F., Hjartardóttir, Á.R., Geirsson, H., Pedersen, G.B.M., Belart, J.M.C., Barsotti, S., Lanzi, C., Vogfjörd, K., Hooper, A., Ófeigsson, B., Hreinsdóttir, S., Gestsson, E.B., Þrastarson, R.H., Einarsson, P., Tolpekin, V., Rotheram-Clarke, D., Gunnarsson, S.R., Óskarsson, B.V., Pinel, V., 2025: 2023–2024 inflation-deflation cycles at Svartsengi and repeated dike injections and eruptions at the Sundhnúkur crater row, Reykjanes Peninsula, Iceland. *Earth Planet. Sci. Lett.*, 658, 119324. doi.org/10.1016/j.epsl.2025.119324.

Pedersen, G.B.M., Belart, J.M.C., Óskarsson, B.V., Gudmundsson, M.T., Gies, N., Högnadóttir, T., Hjartardóttir, Á.R., Pinel, V., Berthier, E., Dürig, T., Reynolds, H.I., Hamilton, C.W., Valsson, G., Einarsson, P., Ben-Yehosua, D., Gunnarsson, A., Oddsson, B., 2022: Volume, effusion rate, and lava transport during the 2021 Fagradalsfjall eruption: Results from near real-time photogrammetric monitoring. *Geophys. Res. Lett.*, 49, e2021GL097125. doi.org/10.1029/2021GL097125.

Persson, H.J., Mukhopadhyay, R., Valbuena, R., Shevchenko, A.V., Lück, L., Herold, M., Motagh, M., Oré, G., Freitas, E., Wimmer, C., Hernandez-Figueroa, H.E., 2024: Setup of a drone-based SAR experiment to analyze a boreal forest. *IGARSS 2024 – 2024 IEEE International Geoscience and Remote Sensing Symposium,* 4535–4538. doi.org/10.1109/IGARSS53475.2024.10640704.

Pinter, N., Casagrande, D., Thorsteinsdottir, G.M., 2026: Managing the Sundhnúkagígar–Grindavík volcanic emergency in Iceland, 2023–2026. *Nat Hazards,* 122, 361. doi.org/10.1007/s11069-026-08084-y.

Rocha, H.S., Góes, J.A., Hernandez-Figueroa, H.E., Moreira, J. 2025: Efficient GPU-Accelerated Ground-Penetrating SAR Tomography for Arbitrary Terrain. *IGARSS 2025 – 2025 IEEE International Geoscience and Remote Sensing Symposium,* 9263–9267. doi.org/10.1109/IGARSS55030.2025.11242534.

Shevchenko, A.V., Dvigalo, V.N., Walter, T.R., Mania, M., Maccaferri, F., Svirid, I.Y., Belousov, A.B., Belousova, M.G., 2020: The rebirth and evolution of Bezymianny volcano, Kamchatka, after the 1956 sector collapse. *Commun. Earth Environ.*, 1, 15. doi.org/10.1038/s43247-020-00014-5.

Shevchenko, A.V., Walter, T.R., Gudmundsson, M.T., Belart, J.M.C., Marzban, P., Zorn, E.U., Sæmundsson, Þ., Helgason, J.K., Turowski, J.M., Vassileva, M.S., Motagh, M., Müller, D., 2024: Morphological changes of the south-eastern wall of Askja caldera, Iceland over the past 80 years. *Commun. Earth. Environ.*, 5, 441. doi.org/10.1038/s43247-024-01616-z.

Troll, V.R., Deegan, F.M., Thordarson, T., Tryggvason, A., Krmíček, L., Moreland, W.M., Lund, B., Bindeman, I.N., Höskuldsson, Á., Day, J.M.D., 2024: The Fagradalsfjall and Sundhnúkur Fires of 2021–2024: A single magma reservoir under the Reykjanes Peninsula, Iceland? *Terra Nova*, 36, 447–456. doi.org/10.1111/ter.12733.

Walter, T.R., Zorn, E.U., González, P.J., Sansosti, E., Muñoz, V., Shevchenko, A.V., Plank, S.M., Reale, D., Richter, N., 2023: Late complex tensile fracturing interacts with topography at Cumbre Vieja, La Palma, *Volcanica,* 6/1, 1–17. doi.org/10.30909/vol.06.01.0117.

Xu, Z., Su, F., Xu, G., 2023: Back projection algorithm based on linear estimation of refraction point position for subsurface imaging in layered scenes, *Proc. SPIE 12557, AOPC 2022: Optical Sensing, Imaging, and Display Technology,* 125570S. doi.org/10.1117/12.2648155.